remote sensing

MDPI

Article

Instrument Overview and Radiometric Calibration Methodology of the Non-Scanning Radiometer for the Integrated Earth–Moon Radiation Observation System (IEMROS)

Hanyuan Zhang [1,2], Xin Ye [1,*], Duo Wu [1], Yuwei Wang [1], Dongjun Yang [1], Yuchen Lin [1,2], Hang Dong [1,2], Jun Zhou [1] and Wei Fang [1]

[1] Changchun Institute of Optics, Fine Mechanics and Physics, Chinese Academy of Sciences, Changchun 130033, China; zhanghanyuan19@mails.ucas.ac.cn (H.Z.); wudo@ciomp.ac.cn (D.W.); wangyuwei@ciomp.ac.cn (Y.W.); yangdongjun@ciomp.ac.cn (D.Y.); linyuchen21@mails.ucas.ac.cn (Y.L.); donghang21@mails.ucas.ac.cn (H.D.); zhoujun@ciomp.ac.cn (J.Z.); fangw@ciomp.ac.cn (W.F.)

[2] School of Optoelectronics, University of Chinese Academy of Sciences, Beijing 100049, China

* Correspondence: yexin@ciomp.ac.cn; Tel.: +86-159-4305-3209

Abstract: The non-scanning radiometer with short-wavelength (SW: 0.2–5.0 μm) and total-wavelength (TW: 0.2–50.0 μm) channels is the primary payload of the Integrated Earth–Moon Radiation Observation System (IEMROS), which is designed to provide comprehensive Earth radiation measurements and lunar calibrations at the L1 Lagrange point of the Earth–Moon system from a global perspective. This manuscript introduces a radiometer preflight calibration methodology, which involves background removal and is validated using accurate and traceable reference sources. Simulated Earth view tests are performed to evaluate repeatability, linearity, and gain coefficients over the operating range. Both channels demonstrate repeatability uncertainties better than 0.34%, indicating consistent and reliable measuring performance. Comparative polynomial regression analysis confirms significant linear response characteristics with two-channel nonlinearity less than 0.20%. Gain coefficients are efficiently determined using a two-point calibration approach. Uncertainty analysis reveals an absolute radiometric calibration accuracy of 0.97% for the SW channel and 0.92% for the TW channel, underscoring the non-scanning radiometer's capability to provide dependable global Earth radiation budget data crucial to environmental and climate studies.

Keywords: remote sensing; Earth radiation budget; radiometer; radiometric calibration

Citation: Zhang, H.; Ye, X.; Wu, D.; Wang, Y.; Yang, D.; Lin, Y.; Dong, H.; Zhou, J.; Fang, W. Instrument Overview and Radiometric Calibration Methodology of the Non-Scanning Radiometer for the Integrated Earth–Moon Radiation Observation System (IEMROS). *Remote Sens.* **2024**, *16*, 2036. https://doi.org/10.3390/rs16112036

Academic Editor: Pablo Rodríguez-Gonzálvez

Received: 12 May 2024
Revised: 1 June 2024
Accepted: 4 June 2024
Published: 6 June 2024

1. Introduction

The Earth radiation budget (ERB) serves as a pivotal force in driving climate change, quantifying the imbalance between incoming total solar radiation (TSR), reflected solar radiation (RSR), and outgoing longwave radiation (OLR) at the top of the atmosphere (TOA) [1,2]. These parameters are classified as essential climate variables (ECVs) and require accurate monitoring [3–5]. The predominant approach for ERB data generation relies on space-based satellite observations, spearheaded by NASA's Cloud and Earth Radiant Energy System (CERES) program. CERES instruments employ two complementary orbits to capture the diurnal cycle and conduct Earth scans with a 20 km footprint [6,7]. Despite their capability to observe the entire Earth from multiple satellite orbits, CERES instruments fall short in delivering spatial coverage of the hemisphere at any given moment or providing uninterrupted temporal coverage of specific scenes [8–10]. The resulting uncertainties in integrated ERB analysis arise from spatial averaging, temporal interpolation of CERES gridded data, and complicated modeling of the radiation field over various scene types for radiance inversion [11–13]. Furthermore, CERES aims for a calibration accuracy of 1% in the RSR and 0.5% in the OLR, achieved through a combination of laboratory and on-orbit calibrations, representing state-of-the-art accuracy. However, correction

of the attenuation experienced by CERES through onboard calibration with tungsten lamps and diffusers is a challenge. Therefore, the prospect of observing the entire Earth with a non-scanning instrument and calibrating instruments using the Moon holds great promise [14,15]. NASA previously deployed the Wide-field-of-view (WFOV) radiometer in the Earth Radiation Budget Experiment (ERBE) mission to observe the hemispheric Earth, but it was decommissioned due to its observing mode and early technological limitations that prevented it from addressing the thermal drift [16].

The Changchun Institute of Optics, Fine Mechanics and Physics, Chinese Academy of Sciences has proposed the Integrated Earth–Moon Radiation Observation System (IEMROS) to enable observation of the Earth from a global viewpoint. The IEMROS consists of a non-scanning radiometer and two multispectral cameras strategically stationed at the Lagrange L1 point of the Earth–Moon system. This setup promises comprehensive data collection, providing both broad and detailed insights into Earth's dynamics. Specifically, the multispectral cameras specialize in unraveling the spectral intricacies of diverse terrestrial landscapes with 10 km spatial resolution and millisecond sampling [17]. Meanwhile, the non-scanning radiometer stands out with its ability to capture the Earth's hemispherical vista and perform integral radiation measurements, benefiting from the considerable distance of 3.27×10^5 km [18] between the Earth and the L1 point, steering clear of regional scanning discrepancies. Such a meticulous design not only bolsters the temporal coherence of the Earth observations but also upholds their spatial seamlessness, which is crucial for mitigating errors linked to regional scanning data fitting. Instruments designed for hemispheric-scale Earth radiation observation, such as the payloads on the Deep Space Climate Observatory (DSCOVR) satellite, are currently limited to observing only the sunlit side of the Earth. Similarly, geostationary satellites can only view approximately one-third of the Earth's entire surface. However, the IEMROS non-scanning radiometer uniquely captures continuous, integrated Earth radiometric data, leveraging the Earth's rotation to achieve complete global coverage [19–21]. Additionally, plans are in place for on-orbit absolute lunar calibrations of the IEMROS instruments at the L1 point. This initiative seeks to tackle ongoing calibration challenges encountered by ERB observing payloads, such as diffuser material degradation and operational variations [22,23].

This manuscript delineates the architecture of the IEMROS non-scanning radiometer prototype, delving into the radiometric calibration methodology involving background removal to eliminate thermal drift and ensure operational efficacy. Additionally, it scrutinizes the radiometric performance derived from laboratory measurements (spatial and spectral evaluations are not included). The structure of this paper is as follows. Section 2 elucidates the instrument's structure and operating principle. Section 3 elaborates on the prelaunch radiometric calibration methods and test procedures. Section 4 presents the prelaunch test results and performance assessments. Section 5 discusses our findings, while Section 6 concludes this paper.

2. Non-Scanning Radiometer Overview

The on-orbit observation mode of the IEMROS non-scanning radiometer is shown in Figure 1a. The non-scanning radiometer takes advantage of the unique conditions for continuously monitoring the Earth's disk at the L1 point. The radiometer's operational protocol is rigorously designed to cycle through a sequence of observing targets: Earth, Moon, onboard calibration sources, and cold space, facilitated by a two-dimensional turntable mechanism. The instrument employs two onboard configurations for on-orbit calibration: a diffuser for RSR calibration and a blackbody for thermal radiation calibration. Moreover, observations facing the Moon are designed to determine changes in radiometer response, utilizing the consistent lunar irradiance as a long-term and stable calibration reference.

The calibration procedure comprises five critical steps, as depicted in Figure 1b. The objective is to establish a model that translates the digital numbers (DNs) into target radiance, considering both the radiometric gain and the offset. Initially, the radiometer captures baseline DN readings of space views to determine the background noise, referred to as the offset. Subsequently, observations of onboard calibration sources and the Moon are conducted to acquire raw DNs encompassing both background and source radiance. Following the separation of the background noise component, the process yields DNs that accurately reflect the source radiance, facilitating regression analysis to determine the radiometric gain. The assessment of the prediction model's confidence interval is supported by the final quantification of the calibration uncertainty. Moreover, the calibration procedure is executed periodically to systematically characterize the response attenuation over time.

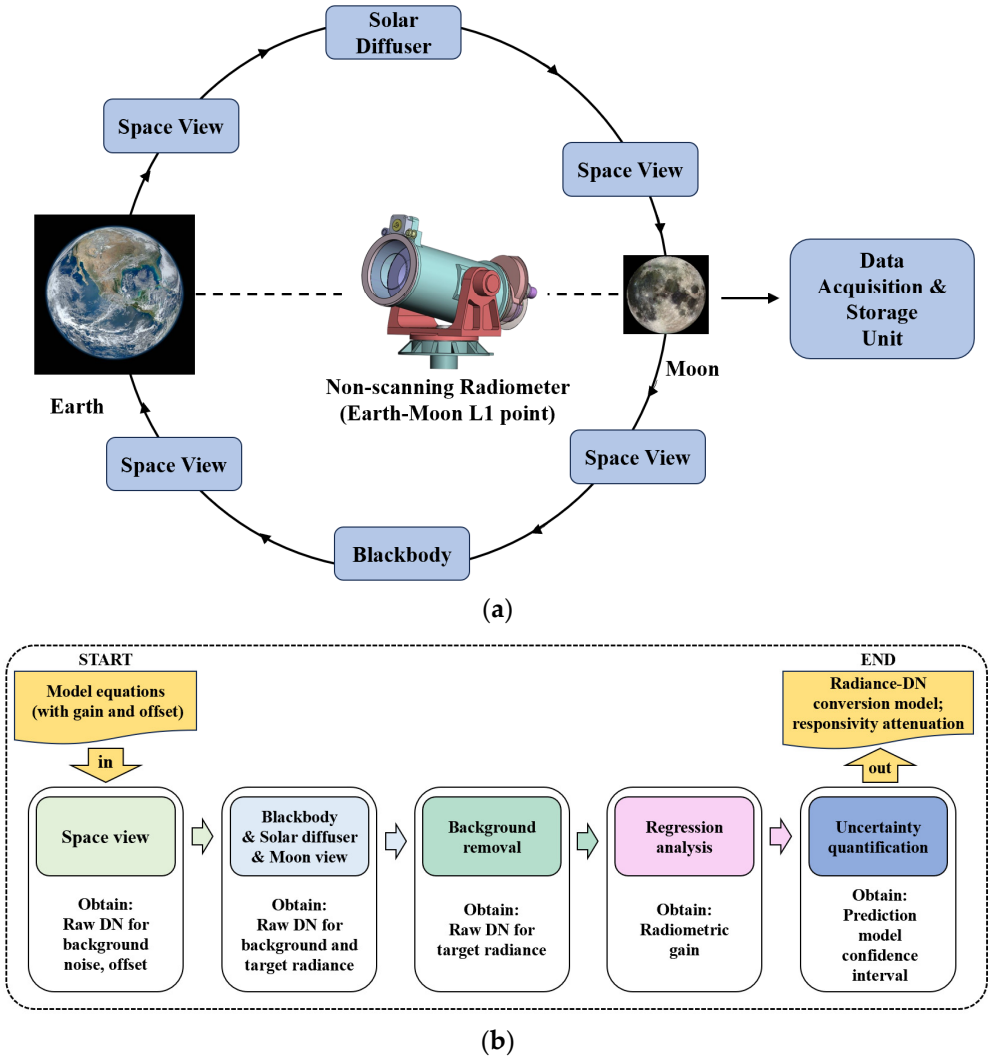

Figure 1. Observation and calibration process of the IEMROS non-scanning radiometer. (**a**) Schematic diagram of the on-orbit observation mode; (**b**) block diagram of the calibration procedure.

2.1. Radiometer Architecture Overview

Key performance requirements of the IEMROS non-scanning radiometer are indicated in Table 1. The non-scanning radiometer, engineered to quantify the Earth's reflected and total radiation, incorporates two specialized channels, each striving for a target calibration accuracy within ±1%. The first, known as the short-wavelength (SW) channel, spans the spectral range of 0.2–5.0 μm. The second, designated as the total-wavelength (TW) channel, covers a broader spectral range of 0.2–50.0 μm. It is crucial to note that the radiometer

calculates the OLR by subtracting data from these two channels. Offering a limb-to-limb view of both the Earth and the Moon, the radiometer updates radiometric data every 5 s, ensuring timely observations and calibration missions. The initial payload is slated to provide continuous Earth radiation measurements for five years.

Table 1. Key performance requirements of the IEMROS non-scanning radiometer.

Parameter	Requirement
Spectral band	0.2–5.0 μm, 0.2–50.0 μm
Radiometric accuracy	±1%
Field of view (FOV)	4°
Sampling time	5s
Measurement repeatability	<0.5%
Nonlinearity	<0.3%
Radiometric stability	±0.5%/year
Pointing accuracy	≤0.1°
Lifetime	5 years
Mass	10 kg

Figure 2a through Figure 2c illustrate the main components of the non-scanning radiometer, providing external, sectional views and a photograph of the prototype, respectively. These include a two-stage baffle, a Cassegrain telescope, a strategically positioned filter wheel for efficient channel switching and weight reduction, essential detector assemblies, and the necessary associated electronics. The SW and TW channels use a shared telescope to project an f/1.1 beam onto the detector. Specifically, the SW channel incorporates a 1-mm-thick fused waterless quartz filter, and the TW channel has no optical filter. The mirrors are made of microcrystalline glass coated with aluminum and supported by invar alloy structures. These mirror materials are selected for their low linear thermal expansion [24,25], which is indispensable for minimizing thermal aberrations and assuring that the telescope maintains a constant focal length despite possible temperature variations.

The radiometer's telescope features an outer baffle, vanes, and an inner baffle that work together to efficiently absorb or deflect stray radiation. The external baffle attenuates the solar radiation, but stray radiation may scatter directly into the backend optical system. To counteract such occurrences, multiple vanes are meticulously arranged within the baffle to create a series of light traps that enhance the absorption of stray radiation and eliminate its direct scattering into the optical path. The baffle houses twenty vanes, with the position of the first vane determined by the entrance diaphragm. The location and height of subsequent vanes are determined by the intersection point where a line from the baffle's base to the inner boundary of the entrance diagram crosses the radiometer's marginal FOV. Consequently, vanes are designed with varying diameters to maintain an unobstructed FOV. The surfaces of the vanes and baffles facing away from the detectors are coated with Nextel Velvet Black Coating 811-21 [26] to optimize external stray light elimination, while others are polished to minimize internal self-emission. The operating temperatures of both the optics and the detectors are carefully controlled at a stable temperature of 292 K, with a tight tolerance of ±0.3 K. To achieve this level of thermal stability, a combination of heaters and passive radiators is employed. The heaters provide active temperature control, while the passive radiators facilitate the dissipation of excess heat. Both approaches guarantee that the radiometer operates within its optimum temperature range.

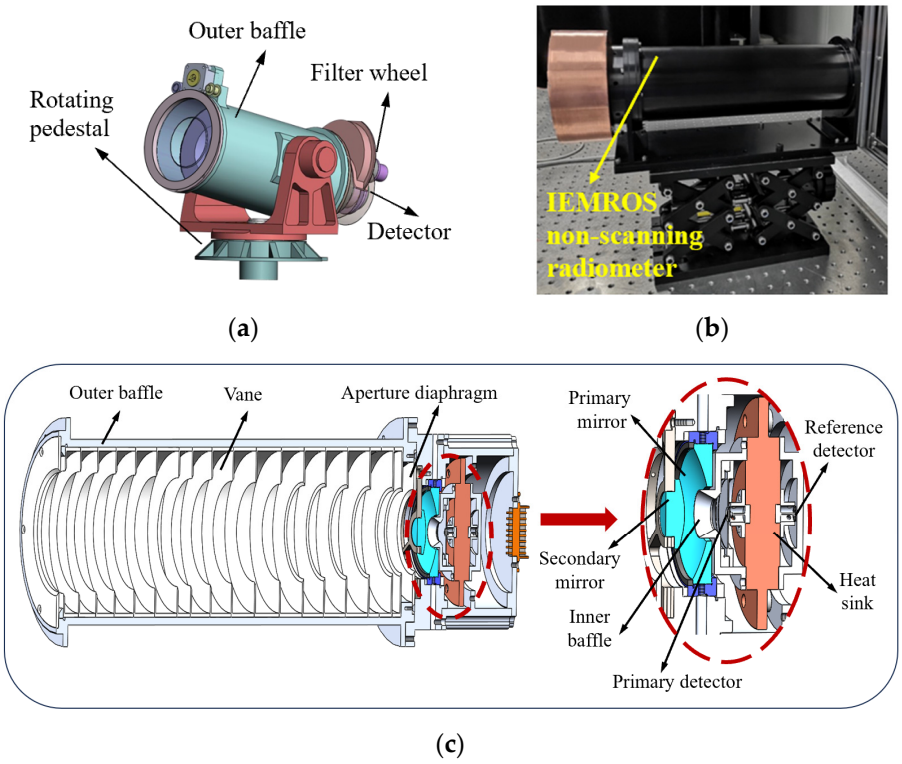

Figure 2. IEMROS non-scanning radiometer. (**a**) External schematic diagram; (**b**) photograph of the prototype; (**c**) schematic of the primary internal structure portion of the prototype, excluding the filter wheel and the external mechanical structure of the entire instrument.

2.2. Detector Module Overview

The IEMROS non-scanning radiometer's pivotal element is the bolometric detector module, which operates based on thermal radiation and conduction principles. The technological basis of such a module has been validated by its application in the spaceborne relative radiometer onboard the Fengyun-3F satellite [27]. Figure 3a,b shows the detector module's schematic diagram and mechanical model. There are four major components: the primary detector, the reference detector, the heat sink, and the heat transfer rod. The primary and reference detectors are mounted on separate thermally coupled disks. These detectors are connected to the heat sink, maintained at a constant temperature, and secured to the enclosure with a polyimide gasket for mechanical stability and thermal isolation. The detectors are coated with Nextel Velvet Coating 811-21, which absorbs the radiation from the target and converts it to heat, resulting in a detectable change in the temperature of the primary detector. The relationship between the detector temperature and the incident radiation is quantified and described by Equation (1), which characterizes the response model of the detector and delineates how changes in radiation levels are translated into temperature changes.

$$P_i = P_e + P_f + P \tag{1}$$

where P_i is the radiation incident on the detector. In Equation (1), the thermal radiation of the receiver P_e is given by:

$$P_e = \varepsilon_1 \sigma S_1 T_1^4 \tag{2}$$

where ε_1 is the emissivity of the receiving surface coating, σ is the Stefan–Boltzmann constant, S_1 is the area of the receiving surface, and T_1 is the receiving surface's temperature.

The heat transfer from the receiver to the rod P_f can be described as:

$$P_f = K_{sh}(T_1 - T_2) \tag{3}$$

where T_2 is the temperature of the heat sink, and K_{sh} is the thermal conductivity of the heat transfer rod.

The increased internal energy of the receiver P_c can be obtained as follows:

$$P_c = Cm_1 \frac{\partial T_1}{\partial t} \tag{4}$$

where C is the heat capacity of the receiving surface, and m is the mass of the detector. When the detector module reaches a steady-state thermal equilibrium, $\partial T_1 / \partial t = 0$. Thus, the variation in T_1 is directly dependent on the incident radiation.

The primary detector in the system is highly sensitive not only to the target radiation but also to the thermal conduction from the radiometer components. Therefore, a reference detector is used to compensate for variations in thermal conduction associated with fluctuations in ambient temperature. Although the reference detector operates in the same environmental conditions as the primary detector, it is not directly exposed to the target radiation. Consequently, by measuring the temperature of the reference detector and comparing it to that of the primary detector, one can effectively discriminate the signal component attributable to target radiation from that caused by ambient temperature changes. Two micro thermistors, each with equal resistance, are embedded in the reserved holes of the heat transfer bar. These thermistors are tasked with independently gauging the temperatures of the primary and reference detectors. As elements of a Wheatstone bridge circuit, these thermistors exhibit a change in thermal resistance that correlates with changes in detector temperature. Such resistance changes are detected by the bridge circuit, which in turn generates a corresponding electrical signal. The signal is then amplified and subjected to differential processing for improved accuracy. Finally, the signal is sampled and digitized for conversion to 16-bit digital counts.

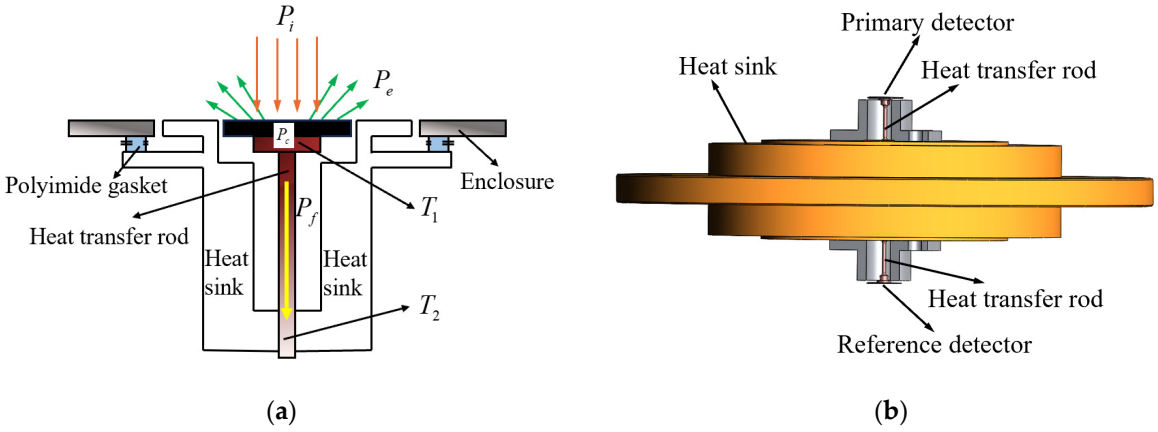

Figure 3. The detector module of the IEMROS non-scanning radiometer. (**a**) Schematic diagram of the detector measurement principle. (**b**) Diagram of the overall structure of the detector module.

3. Methods and Tools

Prior to launch, the non-scanning radiometer performs a comprehensive radiometric characterization and calibration process. This process is designed to verify that the radiometer is operating according to its specified requirements and to gather essential data for future on-orbit calibration efforts. Radiometric calibrations are performed to assess each channel's repeatability, linearity, and gain.

3.1. Calibration Scheme

3.1.1. Background Removal

To elucidate the calibration principle of the non-scanning radiometer, it is critical to understand the methodology for acquiring target signals. As shown in Figure 4, radiation from the observed target is directed into the Cassegrain telescope and then reflected by the mirrors to focus on the primary detector, causing a temperature rise. Nevertheless, according to Planck's law, the radiometer's optical components and structural elements emit radiation because of their temperatures above absolute zero (0 K) [28]. Such self-generated thermal radiation is collected by the primary detector, generating a discernible signal independent of external radiation. Simultaneously, the inherent thermal energy of the detector and associated electronics contributes to a dark signal. Consequently, before converting the output data to target radiance, it is imperative to eliminate the background noise, which encompasses both the self-generated thermal radiation and the dark signal. The constancy of the background noise is maintained through meticulous temperature regulation of both the optics and the detector. Thus, the excision of the background noise constitutes the preliminary phase of calibration.

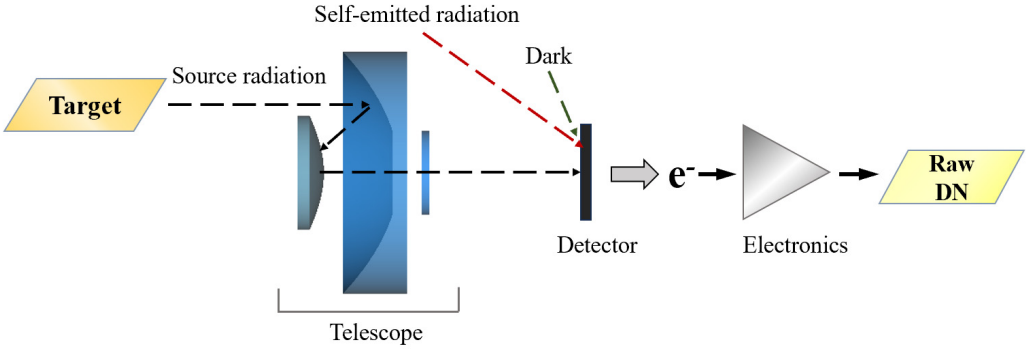

Figure 4. Diagram showing the main radiation pathways reaching the primary detector and producing the raw signal.

Characterization of the radiometer's background noise involves the use of an aluminum shutter. The shutter effectively blocks external radiance by occluding the radiometer's aperture, thereby allowing the radiometer's digital output to contain only the intrinsic thermal and dark noise background. Throughout the characterization and calibration interval, the radiometer cyclically shifts focus between the target and the shutter. Thus, the digital counts derived from the background removal phase reflect exclusively the source signal, while the radiometer maintains thermal and electrical stability. The process is described by Equation (5). During preflight testing, instrument temperature assessments monitor background signal stability, while subsequent in-orbit verification is facilitated by space view observations and temperature telemetry.

$$\begin{aligned} DN_{signal} &= DN_{source\ view} - DN_{background\ view} \\ &= (DN_{source} + DN_{self\text{-}thermal\ radiation} + DN_{dark}) - (DN_{self\text{-}thermal\ radiation} + DN_{dark}) \\ &= DN_{source} + \Delta DN_{self\text{-}thermal\ radiation} + \Delta DN_{dark} \end{aligned} \quad (5)$$

where $\Delta DN_{self\text{-}thermal\ radiation}$ and ΔDN_{dark} represent the potential drift of the radiometer's self-emitted radiation and dark signals due to temperature variations during the observation source and shutter periods, respectively.

3.1.2. Relation to Radiance

The result of the background removal process is the desired source signal, described as background-subtracted counts. These counts are important for assessing the performance of the radiometer and require conversion to the absolute radiance incident at the instrument's aperture. An analysis of the response model linking these elements is performed to

establish a correlation between these signals and the radiance incident on the radiometer, as shown in Figure 5. The analytical process is fundamental to translating the quantitative measurements obtained from the radiometer, after eliminating background noise, into meaningful data that accurately reflect the radiance entering the instrument.

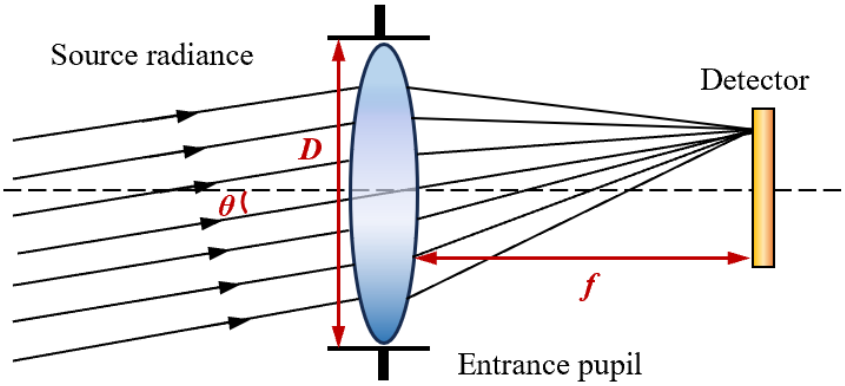

Figure 5. Path of source radiation through the Cassegrain telescope to the primary detector.

The source radiation received by the primary detector can be expressed by Equation (6).

$$\Phi = L_{source} \cdot (\frac{\pi}{4}) D^2 \cdot \cos\theta \cdot \Omega \cdot \tau_{opt} \tag{6}$$

where L_{source} is the uniform radiance entering the optical system, D is the diameter of the entrance pupil, θ is the angle between the incident radiation and the telescope's principal axis, τ_{opt} is the total transmittance of the optical system, and Ω is the radiation solid angle corresponding to the detector receiving area S_1.

The Ω can be calculated as:

$$\Omega = \frac{S_1 \cdot \cos\theta}{(f/\cos\theta)^2} \tag{7}$$

where f is the telescope's focal length.

For the established non-scanning radiometer, the FOV is very small, so $\cos\theta \approx 1$. And S_1, D, f, and τ represent constants. Thus, the relationship between the radiant flux received by the detector and its influencing factors is linear, as described by Equation (8).

$$\Phi_{source} = \frac{\tau_{opt} \cdot \pi \cdot S_1 \cdot D^2 \cdot \cos^4\theta}{4f^2} \cdot L_\lambda = K \cdot L_{source} \tag{8}$$

where K is treated as a constant, $K = \frac{\tau_{opt} \cdot \pi \cdot S_1 \cdot D^2 \cdot \cos^4\theta}{4f^2}$.

According to the working principle of the detector described in Section 2.1, the radiant flux received by the primary detector is proportional to the measured temperature difference. Consequently, this proportionality is mathematically expressed through a linear equation, which converts the source radiance into background-subtracted DN counts, as detailed in Equation (9).

$$L_{source} = G^{-1} \cdot DN_{signal} \tag{9}$$

where G^{-1} is the radiometric gain of the IEMROS non-scanning radiometer.

The correlation between the background-subtracted signal and the incident radiance is quantifiable by observing and documenting the output counts from known radiance calibration sources. The method involves converting all detected counts to their respective expected radiance values over the measured intervals using linear interpolation and regression analysis. Linear interpolation estimates values within the range of the calibration points, while regression analysis provides a statistical method to determine the best-fitting

linear model that describes the relationship. As a result, the digital signal of the radiometer can be converted to the absolute radiance for scientific analysis.

3.2. Testing Equipment

To determine the repeatability and linearity of the SW channel, a radiance-adjustable integrating sphere and a high linearity spectroradiometer are used. Since the spectroradiometer's accuracy falls below 1%, a standard lamp traceable to the National Institute of Standards and Technology (NIST) is employed to attain the target calibration accuracy of ±1% for the SW channel. In parallel, the TW channel is tested for repeatability, linearity, and gain coefficient using a blackbody with a controllable temperature setting, which warrants a thorough evaluation of the radiometer's operational capabilities across all channels.

3.2.1. Integrating Sphere

A 300 mm diameter integrating sphere with a 100 mm exit diameter is provided to test the repeatability and linearity of the non-scanning radiometer's SW channel. Three 35 W tungsten halogen lamps provide illumination within the sphere. The sphere's inner surface is coated with barium sulfate to improve reflectivity. An adjustable diaphragm inside the sphere, controlled by input pulses, changes its diameter to provide 14 levels of radiance output. A cooling unit within the sphere housing maintains a constant temperature near the lamp. The homogeneity error of the output radiance is less than 0.3%, and the stability error is less than 0.1%.

3.2.2. SVC Spectroradiometer

The HR-1024i spectroradiometer from Spectra Vista Corporation (SVC), located in Poughkeepsie, NY, USA, is used to obtain the spectral radiance of the integrating sphere. The total radiance emitted by the integrating sphere is determined by trapezoidal numerical integration. The SVC HR-1024i is a high-resolution, portable field spectroradiometer with a spectral resolution of 1.5 nm in the 400–1000 nm wavelength range. Radiance measurements are interpolated at 1 nm intervals over an extended 350–2500 nm wavelength range using SVC's proprietary software version SVC HR-1024i_PC_V1_23 for extensive analysis [29]. The initial calibration of the SVC HR-1024i spectroradiometer follows standards traceable to the NIST, with subsequent recalibration performed by the National Institute of Metrology, China (NIM) before testing.

3.2.3. NIST-Traceable Standard Lamp

A NIST-traceable standard lamp with a Labsphere diffuser mounted on a precision guide rail is employed for radiometric gain calibration of the SW channel. The NIST lamp is calibrated at the NIST Facility for Automated Spectroradiometric Calibrations (FASCAL 2), ensuring traceability of its irradiance output to international standards [30]. The diffuser transfers the irradiance reference of the lamp to the non-scanning radiometer. The guide rail consistently aligns the lamp at a distance of 500 mm from the diffuser. The manufacturer supplies data for the diffuser's bidirectional reflectance distribution function (BRDF), which contributes to a well-defined calibration process. With the lamp set for direct incidence, the known radiance of the illuminated diffuser at 45° allows for the calibration of the IEMROS non-scanning radiometer in this specific geometry. To eliminate potential measurement disturbances, the entire setup, including the NIST-calibrated lamp, diffuser, and IEMROS non-scanning radiometer, is shielded from any extraneous ambient light, thus preserving the validity of the radiometric calibration. The total radiance of the standard lamp is interpolated and integrated according to the NIST procedure, with an accuracy of better than 0.5% [31–33]. The spectral radiance L_{lamp} after diffusion is given by Equation (10), which provides a mathematical framework for calculating source radiance [34].

$$L_{lamp} = \frac{E_{lamp}(\lambda)}{\pi} \rho_{diffuser}(\lambda) \tag{10}$$

where E_{lamp} is the spectral irradiance of the standard lamp incident on the diffuser, and the $\rho_{diffuser}$ is the spectral BRDF of the diffuser.

3.2.4. ITS-90-Traceable Blackbody

The calibration source for the TW channel is an extended-area blackbody developed and constructed by the NIM. The blackbody has an emissivity of 0.9902, ensuring a high level of radiation emission. It exhibits a temperature homogeneity error of less than 0.06 K. Temperature control of the blackbody is achieved by a DD-200F cooled circulator, which maintains the temperature at the desired level with considerable stability. Temperature measurement and feedback for the blackbody is provided by an internal platinum resistance thermometer (PRT) calibrated at NIM to an uncertainty of ±0.01 K, ensuring highly accurate temperature readings with traceability to the International Temperature Scale of 1990 (ITS-90). The relationship between the radiance emitted by the blackbody and its precisely known temperature is encapsulated in Equation (11).

$$B(\lambda_1, \lambda_2) = \int_{\lambda_1}^{\lambda_2} \frac{c_1}{\lambda^5 [\exp(c_2/\lambda T_{blackbody}) - 1]} d\lambda \tag{11}$$

where λ is the wavelength and C_1 and C_2 are blackbody radiation constants; λ_1 = 0.2 μm, λ_2 = 50.0 μm, C_1 = 3.7417749 × 10^{-16} m·K, and C_2 = 1.438769 × 10^{-2} m·K.

3.3. Test Procedure

For the radiometric characterization and calibration tests, the IEMROS non-scanning radiometer is in the operation state with:

- All detectors are switched on.
- The telescope and the detectors are controlled at the operating temperature of 292 K.
- All instrument science packages are generated (all channels).

Test points for radiometric characterization and calibration are selected taking into account the typical reflected and thermal radiation of the Earth [35]. In concrete terms, given the variation in the Earth's average temperature between 280 K and 330 K [36–38], calibration of the TW channel involves blackbody testing at 2.5 K intervals within this range to ensure adequate sampling and comprehensive coverage of the entire dynamic range. As for the SW channel, the observable RSR is determined by:

$$L^r_{Earth} = \frac{1}{\pi} \alpha E_{Earth} \tag{12}$$

where α represents the Earth's bond albedo, with α = 0.3 [39,40]. Additionally, in the formula for L^r_{Earth}, the solar irradiance on Earth can be calculated as:

$$E_{Earth} = M_{sun} \sin^2 \beta \tag{13}$$

where β represents the view angle of the Sun to the Earth, with β = 16′, and M_{sun} is calculated by treating the Sun as a blackbody at 5900 K [41], employing Equation (11).

From the analysis provided, it is evident that the observable RSR reaches its maximum at approximately 64.71 W·m^{-2}·Sr^{-1}. To incorporate the peak radiance and synchronize it with the adjustable radiance level of the source, 13 test points are selected for the SW channel calibration. These points are distributed relatively evenly spaced, spanning a range from 8.53 W·m^{-2}·Sr^{-1} to 82.33 W·m^{-2}·Sr^{-1}.

4. Results

4.1. Repeatability

Repeatability is a crucial parameter for evaluating the performance of the non-scanning radiometer and gives critical insight into the reliability and measurement accuracy of the system. It also reflects the impact of background noise variations on the radiometer's performance throughout the calibration period. If the background noise is substantially influenced by temperature variations during this time, the repeatability of the radiometer measurements may be reduced.

Internationally, repeatability u_r is defined as the consistency among results from successive measurements carried out under identical conditions. As per the international standards ISO 5725 and ISO 3534 [42,43], the repeatability standard deviation S_R, determined by the Bessel formula, is recognized as the repeatability value [44,45]. Its relative value can be obtained from Equation (14).

$$u_R = \frac{s_R}{\overline{DN}} = \frac{\sqrt{\frac{\sum_{k=1}^{n} (DN_n - \overline{DN})^2}{n-1}}}{\overline{DN}} \tag{14}$$

where n is the total number of repeated measurements, the $\overline{DN}$ is the arithmetic mean of the repeated measurements, and the DN_n is the n-th measurement value.

The designated interval for conducting repeatability assessments of the non-scanning radiometer is set to 30 s, which exceeds the radiometer's sampling period, ensuring a trustworthy evaluation. Research by Shang et al. shows that the Earth's global OLR and RSR exhibit monthly cyclic variations [46]. Consequently, for Earth observations from the L1 point, an averaging period of 5 s for DN values is considered acceptable and adequate for radiance inversion. It is estimated that Earth's radiance varies by less than 0.01% over this short period. The spectral radiance of the integrating sphere under six different input pulses, as measured by the SVC spectroradiometer, is shown in Figure 6a. In parallel, Figure 6b presents the mean background-subtracted counts for the SW channel corresponding to each radiance level provided by the integrating sphere. The SW channel's measurement repeatability uncertainty, as illustrated in Table 2, is documented as 0.34% for a source radiance of 8.53 $W \cdot m^{-2} \cdot Sr^{-1}$. This error margin significantly diminishes to 0.04% as the source radiance increases to 82.13 $W \cdot m^{-2} \cdot Sr^{-1}$.

Table 2. Repeatability uncertainty of the SW channel.

Pulse Counts	Integrating Sphere Radiance ($W \cdot m^{-2} \cdot sr^{-1}$)	Average Counts	SD Counts	u_R
57,000	8.53	40.0	0.14	0.34%
89,000	23.04	109.9	0.16	0.14%
121,000	37.20	179.4	0.12	0.07%
153,000	50.70	246.6	0.12	0.05%
201,000	68.89	335.1	0.15	0.04%
265,000	82.13	398.9	0.21	0.04%

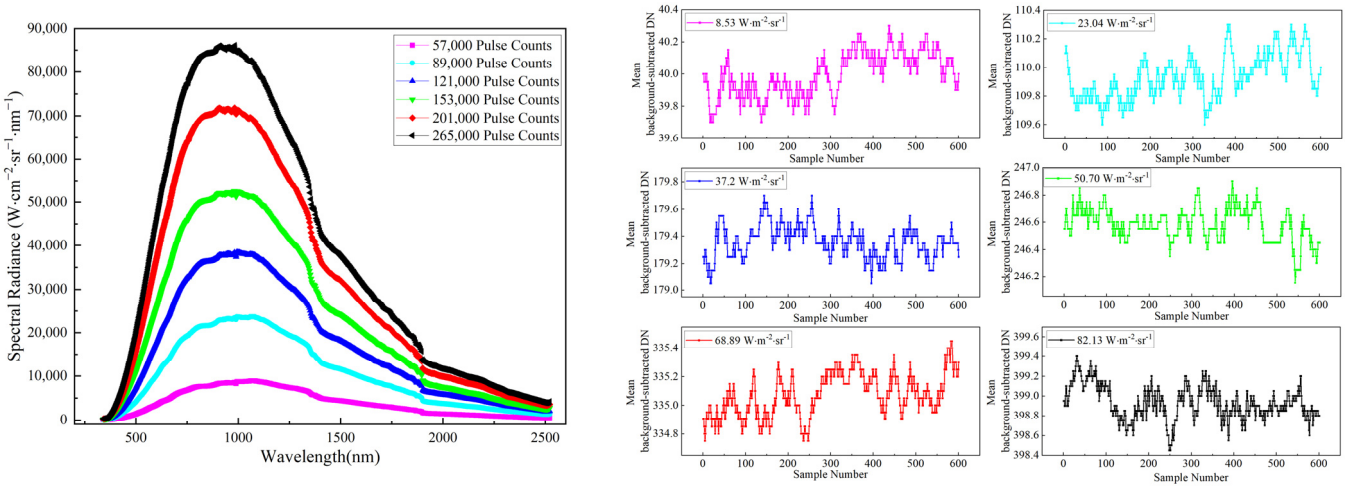

(**a**) (**b**)

Figure 6. (**a**) Spectral radiance output of the integrating sphere measured by the SVC spectroradiometer under different pulse control. (**b**) Mean background-subtracted counts of the SW channel under different radiance of the integrating sphere.

Figure 7 delineates the average background-subtracted counts for the TW channel, observed over blackbody temperatures from 280.01 K to 330.00 K. With increasing temperature, the average counts increase from 509.1 to 994.8, while maintaining a standard deviation below 0.2, indicating a repeatability uncertainty of less than 0.03%. Table 3 details the standard deviation (SD) of the counts and the repeatability uncertainty of the radiometer, further demonstrating a reduction in uncertainty to 0.02% as the temperature approaches 330.00 K. The high repeatability of the non-scanning radiometer not only confirms its precision in measurements but also demonstrates that the internal thermal drift is effectively mitigated, ensuring stability and the accurate reflection of the original signal without interference from background radiation during normal observational activities.

Table 3. Repeatability uncertainty of the TW channel.

Average Blackbody Temperature (K)	Blackbody Radiance ($W \cdot m^{-2} \cdot sr^{-1}$)	Average Counts	SD Counts	u_R
280.01	105.78	509.1	0.18	0.03%
287.50	117.86	567.4	0.16	0.03%
294.99	130.94	630.4	0.17	0.03%
297.50	135.55	652.5	0.13	0.02%
300.00	140.26	674.3	0.17	0.03%
307.49	155.11	747.0	0.12	0.02%
314.99	171.12	823.9	0.14	0.02%
322.50	188.35	906.9	0.19	0.02%
324.99	194.34	935.7	0.10	0.01%
330.00	206.79	994.8	0.17	0.02%

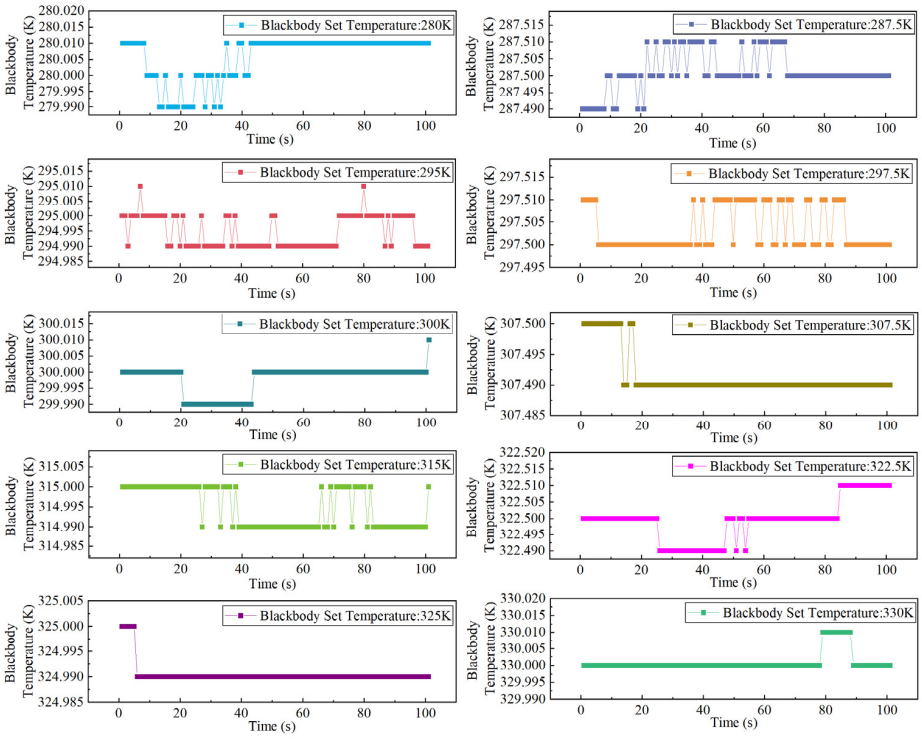

(**a**)

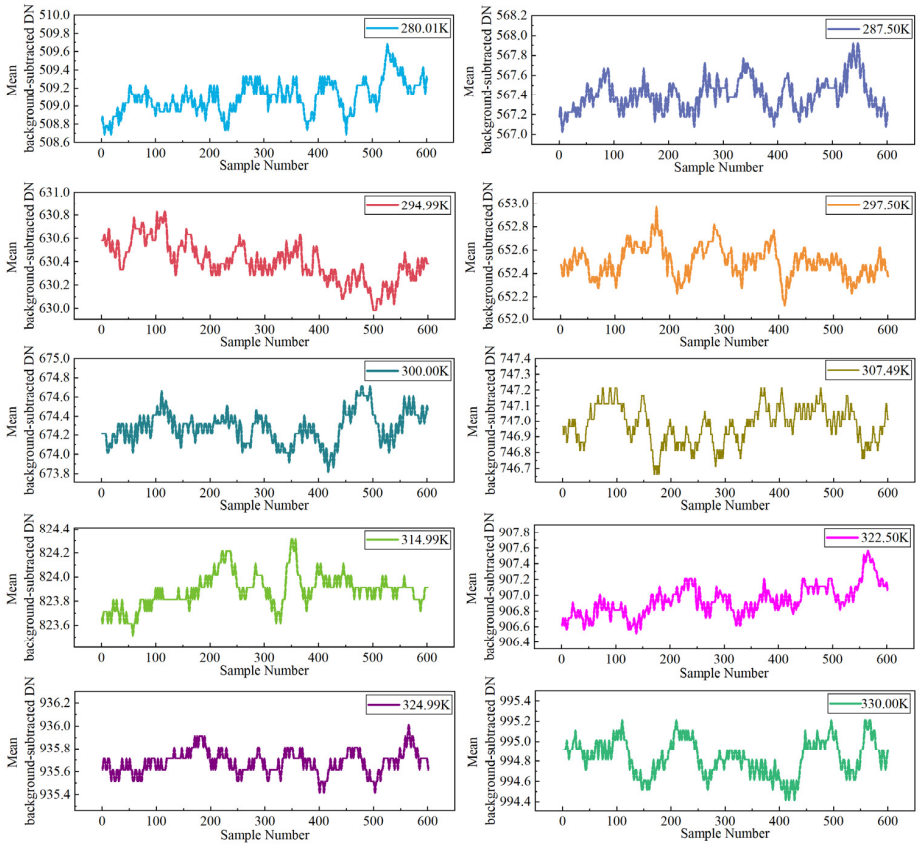

(**b**)

Figure 7. (**a**) Blackbody temperature measured at different settings. (**b**) Mean background-subtracted counts of the TW channel under different blackbody temperatures.

4.2. Linearity

The linearity of the radiometer is rigorously examined through experiments that validate the linear radiation measurement paths of the IEMROS non-scanning radiometer, as detailed in Sections 3.1 and 3.2. Nonlinearity is defined as the relative deviation between the linear approximation and the actual measured response of the radiometer [47]. To quantitatively ascertain the linearity of the non-scanning radiometer, two parameters are employed: the square of the linear correlation coefficient (R^2) and the relative fitting residual (S_L). Linearity evaluations of the SW and TW channels are, respectively, based on observations from an integrating sphere at 14 different radiance levels spanning from 8.53 $W \cdot m^{-2} \cdot Sr^{-1}$ to 82.13 $W \cdot m^{-2} \cdot Sr^{-1}$, and from observations at 21 blackbody temperatures, which are incrementally adjusted by 2.5 K intervals from 280 K to 330 K.

For intuitive linearity analysis, the background-subtracted *DN* values and the corresponding radiances from calibration sources are normalized as follows:

$$DN^i_{normalized} = (DN_i - DN_{\min}) / (DN_{\max} - DN_{\min}) \tag{15}$$

$$\hat{L}^i_{normalized} = (L_i - L_{\min}) / (L_{\max} - L_{\min}) \tag{16}$$

where $DN^i_{normalized}$ is the normalized count under the i-th radiance or temperature level, DN_i is the original count under the i-th radiance or temperature level, and the $\hat{L}^i_{normalized}$ is the normalized and calibrated radiance. Note that these are not physical values, but normalization points.

The relative fitting residual is then calculated using [48]:

$$S_L = \frac{\sqrt{\sum_{i=1}^{M} \left(L^i_{normalized} - \hat{L}^i_{normalized}\right)^2 / M}}{\overline{L}^i_{normalized}} \tag{17}$$

where M is the total number of radiance or temperature levels, $L^i_{normalized}$ is the reference radiance.

Least-squares regression analyses are performed on the normalized radiance and background-subtracted counts for both the SW and TW channels, including a comparative examination of linear, quadratic, cubic, and quartic polynomial regressions. The plots in Figure 8a,b and Figure 9a,b show the results of these fits and the corresponding residual distributions for the SW and TW channels, respectively. These visual representations demonstrate minor discrepancies between linear and higher-order polynomial models. The R^2 is very close to unity when using the linear fit.

The nonlinearity for the SW channel is determined to be 0.20%, as shown in Table 4. Similarly, Table 5 illustrates that the TW channel nonlinearity is 0.17%. Despite a nominal decrease in the relative fit residuals from approximately 0.04% to 0.06% achieved by higher-order polynomial regression, such minor adjustments do not significantly enhance the radiometric calibration accuracy. Consequently, the linear regression model suffices to characterize the responses of both channels, eliminating the need for polynomial overfitting to improve calibration confidence, as confirmed by the analysis presented in Section 3.1.2.

Table 4. SW channel linearity analysis results.

Fitting Model	Fitting Result	R^2	Residual Sum of Squares (RSS)	S_L
Linear Polynomial	$y = 0.998x$	0.999986	2.412×10^{-5}	0.20%
Quadratic Polynomial	$y = 1.003x - 0.005x^2$	0.999974	3.848×10^{-5}	0.68%
Cubic Polynomial	$y = 1.030x - 0.096x^2 + 0.067x^3$	0.999998	1.732×10^{-5}	0.18%
Quartic Polynomial	$y = 1.038x - 0.145x^2 + 0.149x^3 - 0.096x^4$	0.999999	9.873×10^{-6}	0.14%

Table 5. TW channel linearity analysis results.

Fitting Model	Fitting Result	R^2	Residual Sum of Squares (RSS)	S_L
Linear Polynomial	$y = 1.001x$	0.999997	1.251×10^{-5}	0.17%
Quadratic Polynomial	$y = 0.989x + 0.007x^2$	0.999998	1.241×10^{-5}	0.17%
Cubic Polynomial	$y = 0.992x + 0.013x^2 + 0.006x^3$	0.999998	1.082×10^{-5}	0.16%
Quartic Polynomial	$y = 0.990x + 0.064x^2 - 0.110x^3 + 0.061x^4$	0.999996	7.848×10^{-6}	0.13%

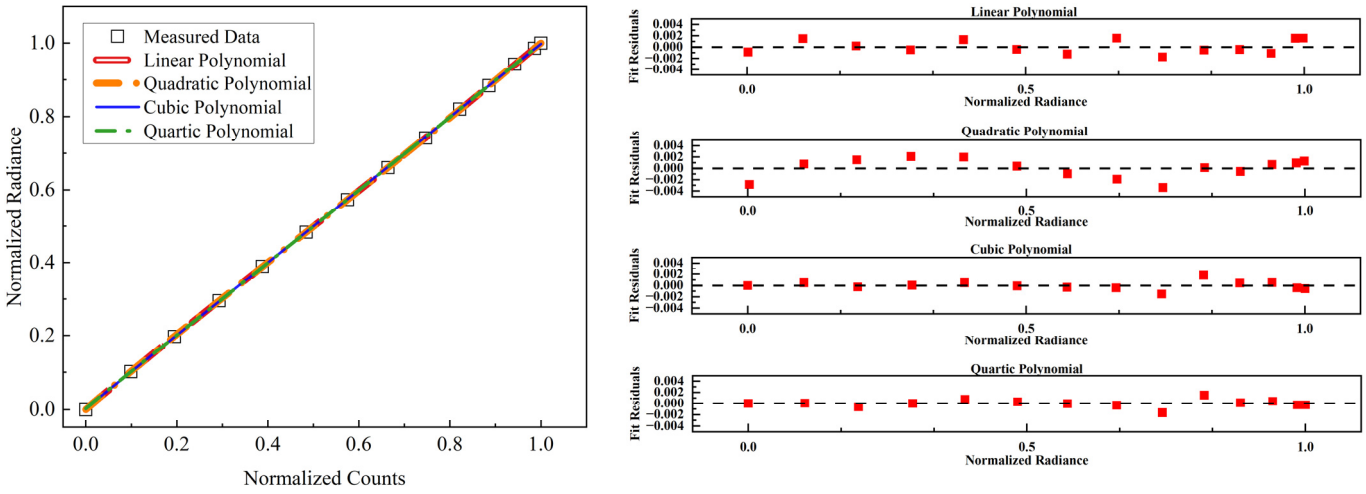

(**a**) (**b**)

Figure 8. (**a**) Four types of fitting curves for the SW channel; (**b**) residual distribution plots of four fitting results for the SW channel.

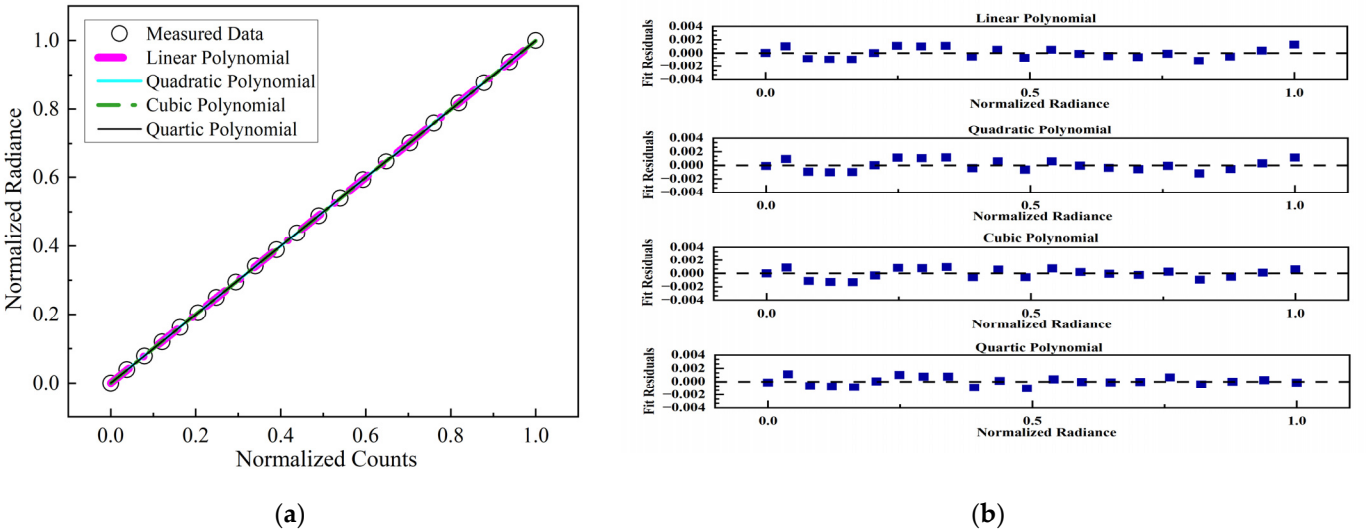

(**a**) (**b**)

Figure 9. (**a**) Four types of fitting curves for the TW channel; (**b**) residual distribution plots of four fitting results for the TW channel.

4.3. Radiometric Gain Coefficient

After evaluating the repeatability and linearity of the IEMROS non-scanning radiometer, gain coefficients are determined for its two channels. The verified linearity of the radiometric response allowed the adoption of a uniform two-point radiometric calibration method for each channel, simplifying the process and ensuring consistency between

channels. The calculation and integration of the total radiance for both the lamp and the blackbody are performed according to Equations (10) and (11), respectively. Figure 10a,b show the final resulting regression lines for both channels, which illustrate that the gain coefficients are 0.19 $W{\cdot}m^{-2}{\cdot}Sr^{-1}{\cdot}count^{-1}$ for the SW channel and 0.21 $W{\cdot}m^{-2}{\cdot}Sr^{-1}{\cdot}count^{-1}$ for the TW channel.

Tables 6 and 7 present a detailed itemization of the uncertainty components involved in the radiometric gain calibration of the IEMROS non-scanning radiometer. The comprehensive uncertainty in the absolute radiometric calibration is derived from contributions related to the calibration source, the reference transfer, and the radiometer's inherent performance metrics. For the SW channel, the identified sources of uncertainty encompass the characterization uncertainty of the standard lamp radiance, the uncertainty associated with the spectral radiance interpolation, the BRDF uncertainty of the diffuser, and the positional uncertainty between the NIST standard lamp and the diffuser.

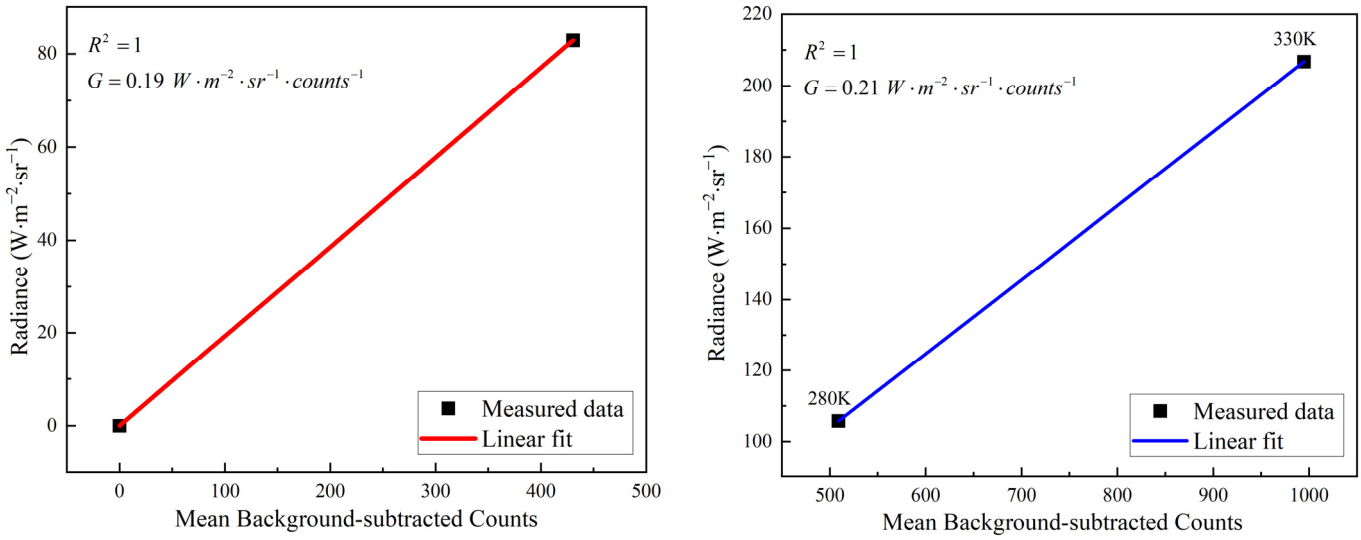

Figure 10. (**a**) Regression analysis result of the SW channel; (**b**) regression analysis result of the TW channel.

Table 6. Absolute radiometric uncertainty of SW channel.

Source of Uncertainty	Relative Standard Uncertainty (%)
NIST lamp uncertainty	0.49
BRDF uncertainty of diffuser	0.6
Distance measurement uncertainty	0.3
Stray light	0.2
Lamp spectral radiance interpolation uncertainty	0.4
Measurement repeatability uncertainty of the IEMROS non-scanning radiometer	0.04
Nonlinearity of the non-scanning radiometer	0.2
Total	0.97

The TW channel's calibration source and radiance reference transfer uncertainties include the blackbody radiance uncertainty, the PRT measurement uncertainty, and the blackbody spectral radiance interpolation uncertainty. The radiometer's own uncertainties are defined by the measurement repeatability uncertainty and the nonlinearity of the instrument. When these elements are combined, the resulting absolute uncertainty is quantified at ±0.97% for the SW channel and ±0.92% for the TW channel. This calculated absolute

uncertainty underlines the precision of the calibration process and guarantees that the measurements of the IEMROS non-scanning radiometer are reliable and accurate within defined limits, thus supporting their application in critical observational and analytical tasks.

Table 7. Absolute radiometric uncertainty of TW channel.

Source of Uncertainty	Relative Standard Uncertainty (%)
Blackbody radiance uncertainty	0.57
PRT measurement uncertainty	0.3
Blackbody spectral radiance interpolation uncertainty	0.4
Stray light	0.5
Measurement repeatability uncertainty of the IEMROS non-scanning radiometer	0.03
Nonlinearity of the non-scanning radiometer	0.17
Total	0.92

5. Discussion

The Integrated Earth–Moon Radiation Observation System (IEMROS) provides a unique capability for Earth observation and lunar calibration from the L1 Lagrange point within the Earth–Moon system. Central to this system is a non-scanning radiometer equipped with dual channels, SW (0.2–5.0 μm) and TW (0.2–50.0 μm), which are crucial for detailed RSR and total radiation measurements. The design of this radiometer aims to enhance Earth Radiation Budget (ERB) analyses by providing spatially and temporally consistent radiation data, thereby reducing uncertainties associated with regional and temporal interpolations. Its architecture encompasses a Cassegrain system, external and internal baffles, a filter wheel, and a detector module identical to that of the Fengyun-3F space-based relative radiometer. Within the detector assembly, a primary detector captures the source radiation, while a reference detector, insulated from direct external radiation, maintains stable thermal conditions. This configuration ensures accurate corrections for ambient temperature variations, thus improving the reliability of measurements. Equipped with a 4° FOV telescope, the radiometer covers the entire lunar disk, facilitating lunar calibration to monitor the radiometer's response attenuation.

A radiometric calibration methodology that eliminates background disturbances, based on rigorous analysis of measurement principles, effectively counters the challenge of thermal drift faced by non-scanning instruments such as the ERBE WFOV radiometer. Tests assessing repeatability, linearity, and gain coefficients for both the SW and TW channels underscore the dependable measurement capabilities of the radiometer. Results indicate that within the specified dynamic range, the measurement repeatability uncertainty for the SW channel is less than 0.34%, and for the TW channel, less than 0.03%, highlighting the stability and consistency of the non-scanning radiometer. Further linear evaluations show a response nonlinearity of 0.20% in the SW channel and 0.21% in the TW channel. Comparisons with high-order polynomial regression fit confirm that linear models sufficiently describe the instrument's radiometric performance, and improvements in calibration accuracy using higher-order polynomial fits are considered insignificant. The high linearity of the non-scanning radiometer facilitates the application of a two-point calibration method to derive gain coefficients, resulting in increased calibration efficiency and consistency between channels. The gain coefficients for both channels, determined through linear regression using data from NIST-traceable lamps and blackbody observations, yield calibration accuracies of ±0.97% for the SW channel and ±0.92% for the TW channel, as verified by the final uncertainty assessment. This demonstrates the precision of the non-scanning radiometer in detecting the Earth's integrated radiance.

Despite the radiometric calibration efforts, we also conducted component-level relative spectral response tests to ascertain the level of out-of-band radiation leakage. Figure 11 displays the filter's transmittance, the mirrors' reflectivity, and the combined relative spectral response of the radiometer across the wavelength range of 0.25 to 25.1 μm. The

data demonstrate that the SW channel effectively blocks radiation in the 5.0–25.1 μm range. While the filter's transmittance properties beyond 25.1–50.0 μm remain indeterminate, the Earth's RSR within this spectral domain is markedly weak, making its influence on the measurement results negligible. The test results confirm that the non-scanning radiometer has reliable radiation collection capabilities within the requisite bandwidth.

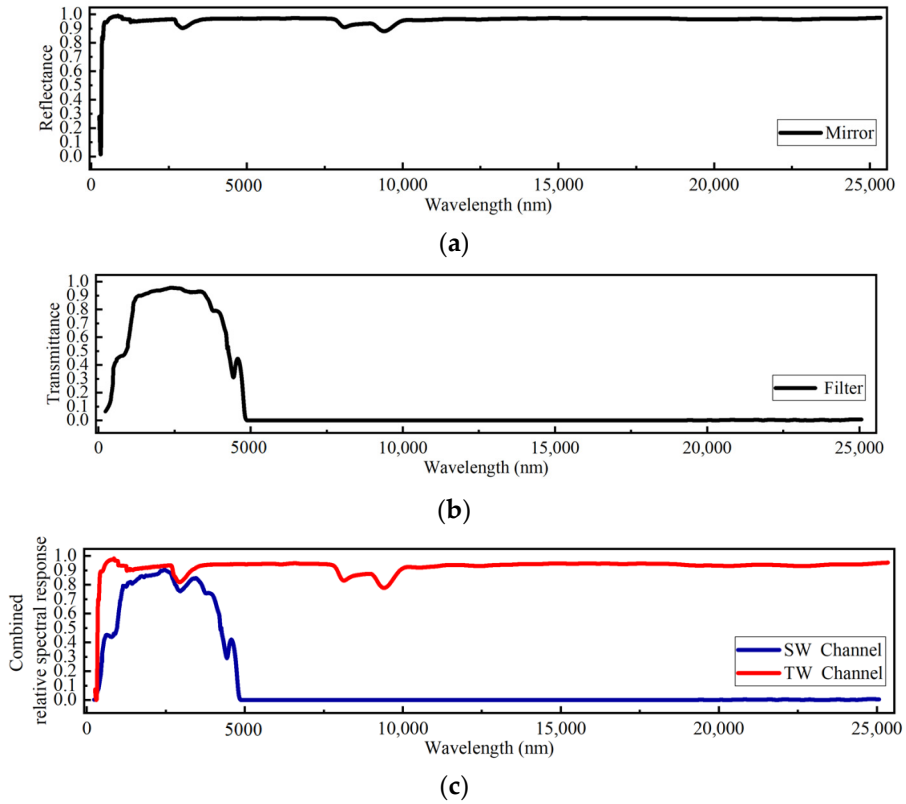

Figure 11. (**a**) Reflectance of the telescope mirror for the IEMROS non-scanning radiometer; (**b**) transmittance of the SW channel filter; (**c**) relative spectral response of SW and TW channels (combined with component-level reflectance and transmittance).

6. Conclusions

Integrated and continuous Earth Radiation Budget (ERB) data are essential for identifying statistically significant, climate-relevant trends and quantifying climate sensitivity. Various errors arise from fitting different temporal and spatial measurement data series during global radiation inversion. Located strategically at the L1 Lagrange point of the Earth–Moon system, the IEMROS non-scanning radiometer is equipped with short-wavelength (SW; 0.2–5.0 μm) and total-wavelength (TW; 0.2–50.0 μm) channels, designed to provide hemispherical radiation measurements of the Earth and facilitate lunar calibration. This paper presents the architecture and operating principles of the IEMROS non-scanning radiometer. A calibration methodology is developed for the radiometer, requiring background noise removal before using linear regression analysis to convert the raw signal into accurate source radiance. This background-removal calibration approach enhances the efficiency of radiometric calibrations and addresses the issue of thermal drift in non-scanning radiometers.

Laboratory radiometric calibration tests focusing on repeatability, linearity, and gain coefficient metrics are conducted before launch, confirming a calibration accuracy of $\pm 0.97\%$ for the SW channel and $\pm 0.92\%$ for the TW channel. The results from these tests confirm that the radiometer can achieve high precision and reliability in detecting Earth's radiance. For the SW channel, the calibration accuracy of $\pm 0.97\%$ ensures that the radiometer can detect and quantify subtle changes in Earth's albedo, including variations caused by cloud

cover, aerosol concentrations, and land-use changes. In practical terms, this means more reliable data for applications such as climate modeling and solar resource assessment. Similarly, the ±0.92% calibration accuracy for the TW channel enables accurate capture of diurnal and seasonal temperature fluctuations, as well as the identification of thermal anomalies that may indicate natural or anthropogenic events. These data are vital for developing performance metrics in Earth observation, such as radiative forcing calculations, energy balance studies, and advanced climate models. Accurate calibration guarantees the reliability of these indicators, enabling more confident decision making in environmental policy and resource management.

The IEMROS non-scanning radiometer enables direct measurement of integrated Earth radiation with a radiometric calibration accuracy exceeding 1%. However, there is still a need to enhance the accuracy of radiometric calibration. In the future, improvements are expected in both the benchmark transfer chain and calibration methodologies, aiming to improve the confidence in the collected data to achieve a radiometric calibration accuracy of 0.3%–0.5%. Additionally, efforts will be made to expand the radiometer's measurement spectrum up to 100.0 μm and to conduct comprehensive instrument-level spectral response evaluations across the entire band. These enhancements will deepen the understanding of Earth's radiative dynamics.

Author Contributions: Conceptualization, X.Y. and H.Z.; methodology, H.Z.; software, D.W.; validation, H.Z., H.D. and Y.L.; formal analysis, H.Z.; investigation, Y.W.; resources, D.Y.; data curation, Y.L.; writing—original draft preparation, H.Z.; writing—review and editing, H.Z. and X.Y.; visualization, X.Y.; supervision, X.Y. and W.F.; project administration, X.Y. and J.Z.; funding acquisition, X.Y. All authors have read and agreed to the published version of the manuscript.

Funding: This research was funded by the Jilin Province Science and Technology Development Plan Project (Grant Number: 20240601033RC). This research was also partly funded by the National Key Research and Development Program of China (Grant Number: 2022YFB3903200, 2022YFB3903201).

Data Availability Statement: The data presented in this study are available on request from the corresponding author. The data are not publicly available due to privacy.

Acknowledgments: The authors thank numerous staff members at the Changchun Institute of Optics, Fine Mechanics and Physics, the Chinese Academy of Sciences, including Kai Wang, Shuqi Li, and Xiaolong Yi. The authors also thank the referees for their generous help and good comments.

Conflicts of Interest: The authors declare no conflicts of interest.

Abbreviations

The following abbreviations are used in this manuscript:

ERB	Earth's radiation budget
TSI	Total solar irradiance
RSR	Reflected solar radiation
ECV	Essential climate variable
WMO	World Meteorological Organization
GCOS	Global Climate Observing System
CERES	Cloud and Earth Radiant Energy System
ERBE	Earth Radiation Budget Experiment
WFOV	Wide field of view
IEMROS	Integrated Earth–Moon Radiation Observation System
DSCOVR	Deep Space Climate Observatory
ADM	Angular distribution model
SW	Short wavelength
TW	Total wavelength
NIST	National Institute of Standards and Technology

SVC	Spectra Vista Corporation
NIM	National Institute of Metrology, China
SD	Standard deviation
RSS	Residual sum of squares
PRT	Platinum resistance thermometer
ITS-90	International Temperature Scale of 1990
ISO	International Organization for Standardization
BRDF	Bidirectional reflectance distribution function

References

1. Ramanathan, V. The role of earth radiation budget studies in climate and general circulation research. *J. Geophys. Res. Atmos.* **1987**, *92*, 4075–4095. [CrossRef]
2. Dewitte, S.; Clerbaux, N. Measurement of the Earth radiation budget at the top of the atmosphere—A review. *Remote Sens.* **2017**, *9*, 1143. [CrossRef]
3. Zemp, M.; Chao, Q.; Han Dolman, A.J.; Herold, M.; Krug, T.; Speich, S.; Suda, K.; Thorne, P.; Yu, W. *GCOS 2022 Implementation Plan*; World Meteorological Organization: Geneva, Switzerland, 2022.
4. Schifano, L.; Smeesters, L.; Geernaert, T.; Berghmans, F.; Dewitte, S. Design and analysis of a next-generation wide field-of-view earth radiation budget radiometer. *Remote Sens.* **2020**, *12*, 425. [CrossRef]
5. Report of the Earth Venture Continuity Radiation Budget Science Working Group. Measurement and Instrument Requirement Recommendations for an Earth Venture Continuity Earth Radiation Budget Instrument. 2018. Available online: https://smd-prod.s3.amazonaws.com/science-red/s3fs-public/atoms/files/ERB_SWG_Rept_FINAL_0.pdf (accessed on 14 May 2020).
6. Green, R.; Wielicki, B.; Coakley, J.; Stowe, L.; Hinton, P.; Hu, Y. Clouds and the Earth's Radiant Energy System (CERES) Algorithm Theoretical Basis Document. CERES Inversion to Instantaneous TOA Fluxes, Release 2. 1997. Available online: https://ceres.larc.nasa.gov/documents/ATBD/pdf/r2_2/ceres-atbd2.2-s4.5.pdf (accessed on 7 September 2023).
7. Priestley, K.J.; Smith, G.L.; Thomas, S.; Matthews, G. Validation protocol for climate quality CERES measurements. In Proceedings of the Infrared Spaceborne Remote Sensing and Instrumentation XV, San Diego, CA, USA, 26–30 August 2007; pp. 389–400.
8. Kato, S.; Loeb, N.G.; Rutan, D.A.; Rose, F.G. Clouds and the Earth's Radiant Energy System (CERES) data products for climate research. *J. Meteorol. Soc. Jpn. Ser. II* **2015**, *93*, 597–612. [CrossRef]
9. Mlynczak, P.E.; Smith, G.L.; Doelling, D.R. The annual cycle of Earth radiation budget from Clouds and the Earth's Radiant Energy System (CERES) data. *J. Appl. Meteorol. Climatol.* **2011**, *50*, 2490–2503. [CrossRef]
10. Barkstrom, B.R.; Smith, G.L. The earth radiation budget experiment: Science and implementation. *Rev. Geophys.* **1986**, *24*, 379–390. [CrossRef]
11. Young, D.; Minnis, P.; Doelling, D.; Gibson, G.; Wong, T. Temporal interpolation methods for the Clouds and the Earth's Radiant Energy System (CERES) experiment. *J. Appl. Meteorol. Climatol.* **1998**, *37*, 572–590. [CrossRef]
12. Loeb, N.G.; Wielicki, B.A.; Doelling, D.R.; Smith, G.L.; Keyes, D.F.; Kato, S.; Manalo-Smith, N.; Wong, T. Toward optimal closure of the Earth's top-of-atmosphere radiation budget. *J. Clim.* **2009**, *22*, 748–766. [CrossRef]
13. Wielicki, B.A.; Barkstrom, B.R.; Baum, B.A.; Charlock, T.P.; Green, R.N.; Lee Iii, R.B.; Minnis, P.; Smith, G.L.; Coakley, J.A.; Randall, D.R. *Clouds and the Earth's Radiant Energy System (CERES) Algorithm Theoretical Basis Document*; National Aeronautics and Space Administration, Langley Research Center: Hampton, VA, USA, 1995.
14. Swartz, W.H.; Dyrud, L.P.; Wiscombe, W.J.; Lorentz, S.R.; Papadakis, S.J.; Wu, D.L.; Summers, R.A.; Wells, V.E. *Measuring Earth's Radiation Imbalance with RAVAN: A CubeSat Mission to Measure the Driver of Global Climate Change*; American Geophysical Union: Washington, DC, USA, 2013.
15. Wong, T.; Smith, G.L.; Kato, S.; Loeb, N.G.; Kopp, G.; Shrestha, A.K. On the lessons learned from the operations of the ERBE nonscanner instrument in space and the production of the nonscanner TOA radiation budget data set. *IEEE Trans. Geosci. Remote Sens.* **2018**, *56*, 5936–5947. [CrossRef]
16. Luther, M.R.; Cooper, J.E.; Taylor, G.R. The Earth radiation budget experiment nonscanner instrument. *Rev. Geophys.* **1986**, *24*, 391–399. [CrossRef]
17. Zhang, H.; Ye, X.; Wang, Y.; Wu, D.; Yang, D.; Fang, W. Aperture division multispectral camera for the Earth's reflected solar radiation observation based on the Lagrange L1 point of the Earth-Moon system. *Opt. Express* **2023**, *31*, 38077–38096. [CrossRef] [PubMed]
18. Zhang, H.; Ye, X.; Zhu, P.; Fang, W.; Wang, Y. Observation system design and analysis for a new staring Earth radiation budget radiometer based on the Lagrange L1 point of the Earth–Moon system. *Remote Sens.* **2022**, *14*, 1596. [CrossRef]
19. Burt, J.; Smith, B. Deep space climate observatory: The DSCOVR mission. In Proceedings of the 2012 IEEE Aerospace Conference, Big Sky, MT, USA, 3–10 March 2012; pp. 1–13.
20. Marshak, A.; Herman, J.; Adam, S.; Karin, B.; Carn, S.; Cede, A.; Geogdzhayev, I.; Huang, D.; Huang, L.-K.; Knyazikhin, Y. Earth observations from DSCOVR EPIC instrument. *Bull. Am. Meteorol. Soc.* **2018**, *99*, 1829–1850. [CrossRef] [PubMed]
21. Hamill, P. Atmospheric observations from the moon: A lunar earth-observatory. In Proceedings of the 2016 IEEE International Geoscience and Remote Sensing Symposium (IGARSS), Beijing, China, 10–15 July 2016; pp. 3719–3722.

22. Stone, T.C.; Kieffer, H.; Lukashin, C.; Turpie, K. The Moon as a climate-quality radiometric calibration reference. *Remote Sens.* **2020**, *12*, 1837. [CrossRef]
23. Jing, Z.; Hu, X.; Wang, Y.; Wu, R.; Chen, L.; Zhang, L.; Huang, Y.; Wang, S.; Li, S.; Zhang, P. Activities to Promote the Moon as an Absolute Calibration Reference. *Remote Sens.* **2023**, *15*, 2431. [CrossRef]
24. Huang, L.; Zhou, Y.; Guo, T.; Han, D.; Gu, Y.; Song, C.; Pan, F. Investigation of Temperature-Dependent Magnetic Properties and Coefficient of Thermal Expansion in Invar Alloys. *Materials* **2022**, *15*, 1504. [CrossRef] [PubMed]
25. Browder, J.S.; Ballard, S.S. Thermal Expansion Measurements on Four Optical Materials from Room Temperature to 10 K. *Appl. Opt.* **1972**, *11*, 841–843. [CrossRef]
26. Kwor, E.T.; Mattei, S. Emissivity measurements for Nextel Velvet Coating 811-21 between-36 °C and 82 °C. *High Temp. High Press.* **2001**, *33*, 551–556. [CrossRef]
27. Wu, D.; Fang, W.; Wang, K.; Ye, X.; Jia, R.; Yang, D.; Song, B.; Luo, Z.; Wang, Y.; Xia, Z. Spaceborne Relative Radiometer: Instrument Design and Preflight Test. *Remote Sens.* **2023**, *15*, 3085. [CrossRef]
28. Montanaro, M.; Lunsford, A.; Tesfaye, Z.; Wenny, B.; Reuter, D. Radiometric calibration methodology of the Landsat 8 thermal infrared sensor. *Remote Sens.* **2014**, *6*, 8803–8821. [CrossRef]
29. Rammeloo, C.; Baumgartner, A. Spectroradiometer Calibration for Radiance Transfer Measurements. *Sensors* **2023**, *23*, 2339. [CrossRef] [PubMed]
30. Ohno, Y.; SP250, S. NIST measurement services: Photometric calibrations. *NIST Spec. Publ.* **1997**, *250*, 37.
31. Huang, L.; Cebula, R.; Hilsenrath, E. New procedure for interpolating NIST FEL lamp irradiances. *Metrologia* **1998**, *35*, 381. [CrossRef]
32. Yoon, H.W.; Gibson, C.E. Spectral Interpolations and Distance Dependences of NIST Spectral Irradiance Standards. 2013. Available online: https://digitalcommons.usu.edu/calcon/CALCON2013/All2013Content/18/ (accessed on 9 October 2023).
33. Ye, X.; Yi, X.; Lin, C.; Fang, W.; Wang, K.; Xia, Z.; Ji, Z.; Zheng, Y.; Sun, D.; Quan, J. Instrument Development: Chinese Radiometric Benchmark of Reflected Solar Band Based on Space Cryogenic Absolute Radiometer. *Remote Sens.* **2020**, *12*, 2856. [CrossRef]
34. Li, S.; Li, C.; Xu, S.; Zhang, H.; Zheng, Y. Preflight radiometric calibration of a carbon dioxide spectrometer. *Meas. Sci. Technol.* **2019**, *30*, 055401. [CrossRef]
35. Kiehl, J.T.; Trenberth, K.E. Earth's annual global mean energy budget. *Bull. Am. Meteorol. Soc.* **1997**, *78*, 197–208. [CrossRef]
36. Sobrino, J.A.; Julien, Y.; García-Monteiro, S. Surface temperature of the planet earth from satellite data. *Remote Sens.* **2020**, *12*, 218. [CrossRef]
37. Valipour, M.; Bateni, S.M.; Jun, C. Global surface temperature: A new insight. *Climate* **2021**, *9*, 81. [CrossRef]
38. Williams, D.M.; Pollard, D. Earth-like worlds on eccentric orbits: Excursions beyond the habitable zone. *Int. J. Astrobiol.* **2002**, *1*, 61–69. [CrossRef]
39. Shukure, N.T.; Tessema, S.B.; Gopalswamy, N. Total Solar Irradiance Variability on the Evolutionary Timescale and its Impact on the Earth's Mean Surface Temperature. *Astrophys. J.* **2021**, *917*, 86. [CrossRef]
40. Kraus, S.F. Measuring the Earth's albedo with simple instruments. *Eur. J. Phys.* **2021**, *42*, 035604. [CrossRef]
41. Fest, E. *Stray Light Analysis and Control*; SPIE Press: Bellingham, WA, USA, 2013; Volume PM229, pp. 1–212.
42. *ISO 5725*; Accuracy (Trueness and Precision) of Measurement Methods and Results. International Organization for Standardization: Geneva, Switzerland, 1994.
43. *ISO 3534-2*; Statistics—Vocabulary and Symbols—Part 2: Applied Statistics. International Organization for Standardization: Geneva, Switzerland, 2006.
44. Zanobini, A.; Sereni, B.; Catelani, M.; Ciani, L. Repeatability and reproducibility techniques for the analysis of measurement systems. *Measurement* **2016**, *86*, 125–132. [CrossRef]
45. Velychko, O.; Gordiyenko, T. The estimation of the measurement results with using statistical methods. In Proceedings of the Journal of Physics: Conference Series, Madeira, Portugal, 3–5 September 2015; p. 012017.
46. Shang, H.; Ding, Y.; Guo, H.; Liu, G.; Liu, X.; Wu, J.; Liang, L.; Jiang, H.; Chen, G. Simulation of Earth's outward radiative flux and its radiance in moon-based view. *Remote Sens.* **2021**, *13*, 2535. [CrossRef]
47. Smith, D.; Barillot, M.; Bianchi, S.; Brandani, F.; Coppo, P.; Etxaluze, M.; Frerick, J.; Kirschstein, S.; Lee, A.; Maddison, B. Sentinel-3A/B SLSTR pre-launch calibration of the thermal infrared channels. *Remote Sens.* **2020**, *12*, 2510. [CrossRef]
48. Xu, N.; Niu, X.; Hu, X.; Wang, X.; Wu, R.; Chen, S.; Chen, L.; Sun, L.; Ding, L.; Yang, Z. Prelaunch calibration and radiometric performance of the advanced MERSI II on FengYun-3D. *IEEE Trans. Geosci. Remote Sens.* **2018**, *56*, 4866–4875. [CrossRef]